Supporting Information

Achieving Ultrahigh Uranium/Vanadium Selectivity of Poly(amidoxime) via Coupling MXene-Enabled Strong Intermolecular Interaction and Separated Photothermal Interface

Hao Ye[a], Ming-Bang Wu[ab*], Qi-Hui Ye[a], Rou-Ming Wen[a], Zhang-Ting Hu[a], Juming Yao[abc*], Chao Zhang[de*]

[a]School of Materials Science and Engineering, Zhejiang Sci-Tech University, Hangzhou 310018, China

[b]Zhejiang Provincial Innovation Center of Advanced Textile Technology, Shaoxing 312000, China

[c]School of Materials Science and Chemical Engineering, Ningbo University, Ningbo 315211, China

[d]MOE Key Laboratory of Macromolecular Synthesis and Functionalization, and Key Laboratory of Adsorption and Separation Materials & Technologies of Zhejiang Province, Department of Polymer Science and Engineering, Zhejiang University, Hangzhou, 310027, China

[e]The "Belt and Road" Sino-Portugal Joint Lab on Advanced Materials, International Research Center for X Polymers, Zhejiang University, Hangzhou, 310027, China

E-mails: wumingbang@zstu.edu.cn (M.-B. Wu), yaoj@zstu.edu.cn (J. M. Yao) zhangchao7@zju.edu.cn (C. Zhang)

1. Materials

Balsa woods were used as the raw materials of wood sponges from Decci Technology Co., Ltd (China). Sodium chlorite ($NaClO_2$, 80%), sodium hydroxide (NaOH, 95%), glacial acetic acid (CH_3COOH, 99.5%), lithium fluoride (LiF, 99%), hydroxylamine hydrochloride ($NH_2OH{\cdot}HCl$, 99%), sodium carbonate (Na_2CO_3, 99.9%) and sodium bicarbonate ($NaHCO_3$, 99.5%) were purchased from Shanghai Macklin Biochemical Technology Co., Ltd (China). Iron (III) nitrate nonahydrate [$Fe(NO_3)_3{\cdot}9H_2O$, 98.5%], cobalt nitrate hexahydrate [$Co(NO3)_2{\cdot}6H_2O$, 99%], nickel chloride ($NiCl_2$, 99%), zinc chloride ($ZnCl_2$, 98%), lead chloride ($PbCl_2$, 99.5%), magnesium chloride ($MgCl_2$, 99%), calcium chloride ($CaCl_2$, 99%) and sodium chloride (NaCl, 99.5%) were obtained from Shanghai Aladdin Biochemical Technology Co., Ltd (China). Ti_3AlC_2 was purchased from Jilin 11 Technology Co., Ltd (China). Hydrochloric acid (HCl, 99%) was purchased from Wuxi Shuanglin Chemical Co., Ltd (China). Ethyl alcohol, N,N-Dimethylformamide (DMF) and glycerol were bought from Zhejiang Tengyu New Material Technology Co. Ltd (China). Polyacrylonitrile (PAN, M_w = 150000, 99%) was supplied by Basf GMBH of Germany. Uranium hexahydrate nitrate [$UO_2(NO_3)_2{\cdot}6H_2O$] was provided by Beijing HWRK Chem Co., Ltd (China).

2. Characterization

Fourier infrared spectrometer (FTIR, Nicolet iS 10, USA) and X-ray photoelectron spectrometer (XPS, Thermo Kalpha, USA) were used for characterizing the chemical structures. The microstructures and elemental mappings were captured via scanning electron microscopy (SEM, Zeiss Gemini 300, Germany). X-ray diffracrometer (XRD, X'Pert PRO MPD, Netherlands) was conducted to determine the crystal structures. The

absorbances, reflectance and transmittances were obtained by UV-vis-NIR spectrophotometer (Hitachi UH4150, Japan). The temperature changes were recorded by Thermal imager (Fluke Tis 55+, USA). Inductively coupled plasma optical emission spectrometer (ICP-OES, PerkinElmer 8300, USA) and inductively coupled plasma-mass spectrometer (ICP-MS, PerkinElmer NexION 300X, USA) were chosen for quantification of metal ion contents. Contact angle meter (Dataphysics OCA20, Germany) was used to measure the contact angles of glycerite. Water contact angle was measured by a contact angle goniometer (Dataphysics OCA20, Germany).

3. DFT Calculations

We used the DFT as implemented in the Vienna Ab initio simulation package (VASP) in all calculations[1]. The exchange-correlation potential is described by using the generalized gradient approximation of Perdew-Burke-Ernzerhof (GGA-PBE)[2]. The projector augmented-wave (PAW)[3] method is employed to treat interactions between ion cores and valence electrons. The plane-wave cutoff energy was fixed to 500 eV. Given structural models were relaxed until the Hellmann–Feynman forces smaller than -0.02 eV/Å and the change in energy smaller than 10^{-5} eV was attained. The MXene model utilized for computations features a 5×5 supercell. The thickness of the plate employed in the study is a minimum of four atomic layers, ensuring comprehensive consideration of periodic effects upon amalgamation with hydrazine. The vacuum thickness was set to be 25 Å to minimize interlayer interactions. During the relaxation, the Brillouin zone was represented by a Γ centered k-point grid of 6×6×1. Grimme's DFT-D3 methodology was used to describe the dispersion interactions among all the atoms in adsorption models[4]. Employing the climbing image nudged

elastic band method (CI-NEB), we computed the minimum energy pathway of the cyclization reaction along with its corresponding activation barrier.

The binding energy (E_{bind}) of a complex formed between two molecules, A and B, can be calculated using the following equation:

$$E_{bind} = (E_A + E_B) - E_{complex} \quad (1)$$

Where $E_{complex}$ is the total energy of the molecular complex of A and B. E_A and E_B are the total energies of isolated molecules A and B, respectively.

4. Experimental Section

4.1 Fabrication of MXene Nanosheets

LiF (2 g) was added into the HCl (9 mol/L, 40 mL) solutions for 30 min. Ti_3AlC_2 (2 g) was then poured slowly into the above solutions at 35 ℃ for 24 h. Subsequently, the dispersion was centrifuged at 3500 rpm for 10 min, washed with water, and recentrifuged until the pH value is about 6. Then, the obtained sediment was exfoliated via sonicating in an ice-bath ethyl alcohol. After sonication for 1 h, the suspension was centrifuged at 3500 rpm for another 1 h. Finally, the MXene nanosheets were obtained via collecting the supernatant.

4.2 Fabrication of Polyamidoxime (PAO)

Firstly, $NH_2OH{\cdot}HCl$ (3.9 g) was completely dissolved into 40 mL of DMF solution at 45 ℃. Then, $NaHCO_3$ (2.69 g) and NaOH (0.7 g) were slowly added and the pH value was adjusted to 7. PAN (2.96 g) was added to the above mixture for more than 90 min. The mixture was heated to 65 ℃ and maintained for 24 h. The obtained white emulsion was centrifuged several times. The PAO was collected by dripping the solutions into ultrapure water.

4.3 Fabrication of Wood Aerogel

Firstly, the pH value of $NaClO_2$ solution (2 wt%) was adjusted to 4.6 by glacial acetic acid, Natural balsa woods with sizes of 1 cm × 1 cm × 5 cm were immersed into the $NaClO_2$ solution at 80 ℃ for 24-48 h to completely remove the lignin. Subsequently, the treated balsa woods were submerged in NaOH solution (8 wt%) at 80 ℃ for another 8 h to remove the hemicellulose. Finally, the wood aerogels were washed by ultrapure water and then freeze-dried for 48 h.

4.4 Fabrication of PAO/MXene@WN

The wood aerogels were thoroughly submerged in the MXene dispersion (1, 2, 4, 5 mg/mL) for 12 h at room temperature. The wood aerogels were taken out and freeze-dried. The balsa wood aerogels decorated with MXene nanosheets (MXene@WN) were then transferred to the PAO solution (1, 2.5, 5, 10 mg/mL) for another 12 h and freeze-dried to obtain the PAO/MXene@WN.

4.5 Batch Adsorption

A 500 ppm of uranium (U) and vanadium (V) aqueous solution was prepared by dissolving $UO_2(NO_3)_2 \cdot 6H_2O$ as well as $VOSO_4 \cdot xH_2O$ into ultrapure water. The pH value was adjusted by HNO_3 (0.1 mol/L) and NaOH (0.1 mol/L). The samples were put into 1 L of U&V-spiked simulated seawater (8 mg/L) under simulated sunlight or dark atmosphere. The concentration changes were measured using ICP-OES after adsorption. Meanwhile, the adsorption capacity was calculated by the following equation:

$$q_t = \frac{(C_0 - C_t) \times V}{m}$$

(2)

where C_0 (mg/L) and C_t (mg/L) are U or V concentrations at initial and t time, respectively. V (L) is the volume of solution while m (g) is the weight of adsorbent.

4.6 Dynamics Adsorption

The samples were floated at the surfaces of U and V-spiked simulated seawater with different concentrations (1, 4, 8, 16 and 32 mg/L) under simulated sunlight. The concentration changes of U and V were analyzed by ICP-OES. Besides, the data obtaining from adsorption in 8 mg/L of U&V solution were then fitted into the intraparticle diffusion model (3):

$$q_t = k_p t^{1/2} + C \quad (3)$$

where q_t (mg/g) is the U or V adsorption capacity at t time; k_p (g/mg/min) is the diffusion rate constant. C is a constant value of the interface layer.

4.7 Thermodynamic Adsorption

The adsorption capacities were measured at 298.15 K, 306.15 K and 313.15 K, respectively. The thermodynamic behavior was determined by calculating the enthalpy changes (ΔH, kJ/mol), standard entropy changes (ΔS, J/(mol·K)), and Gibbs free energy (ΔG, kJ/mol)) by Van't Hoff equations:

$$K_d = \frac{q_e}{C_e} \quad (4)$$

$$\ln K_d = \frac{\Delta S}{R} - \frac{\Delta H}{RT} \quad (5)$$

$$\Delta G = -RT\ln K_d \quad (6)$$

$$\Delta G = \Delta H - T\Delta S \quad (7)$$

where K_d (mL/g) is the Van't Hoff constant, R (8.314 J/mol/K) is the gas constant, T (K) is solution temperature, q_e (mg/g) and C_e (mg/L) are the adsorption capacity and concentration at equilibrium time, respectively.

4.8 Selective Adsorption

The spiked seawater with various coexisting ions was prepared, in which the concentrations of U, V, Fe, Co, Ni, Cu, Zn and Pb ions were 100 times higher than that in the natural seawater. Moreover, Na, Mg, and Ca ion concentrations were identical to those in natural seawater. The adsorbent was placed in 1 L of spiked seawater with coexisting ions for 48 h. Then, the concentration changes were analyzed by ICP-OES.

4.9 Uranium Extraction from Simulated Natural Seawater

A homemade recycling device was used for the uranium extraction from simulated natural seawater. The sample was floated at the surfaces of 6.5 gallons of simulated natural seawater. The flow rate was controlled at 6 gallons/h. Meanwhile, the concentrations of major metal ions in simulated natural seawater were as same as that in the natural seawater. The concentration was measured by ICP-MS per 5 days.

4.10 Antibacterial Test

S. aureus and *E. coli* were dropped into the solid medium and then transferred to a bacterial incubator (temperature: 37 °C, oscillation rate: 120 rpm) for 12 h. The bacterial colonies were then collected into PBS buffer using inoculation loops. Subsequently, the concentrations of the above bacterial solution were diluted to 10^5 CFU/mL using the gradient dilution method. The samples were added into the bacterial

solution (10^5 CFU/mL, 5 mL), followed by co-incubation for 12 h. Then, the above solution (0.1 mL) was dropped into a solid medium and incubated for 12 h. The sterilization rate (%) was calculated by the following equation:

$$Sterilization\ rate = \frac{C_0 - C_t}{C_0} \tag{8}$$

where C_0 and C_t are bacterial concentrations at initial time and t time, respectively.

4.11 Solar Vapor Generation

The solar vapor generation was carried out under simulated sunlight by a Xenon lamp light source (PL-X500D, Beijing Princeton Technology Co. Ltd, China) equipped with an output light source intensity of 1 KW/m^2. The water evaporation rate was obtained by measuring the changes of water mass by electronic balance per 60 min. The photothermal conversion efficiency (η) can be calculated by the following equation:

$$\eta = \frac{\dot{m}E_W}{P_0 C_{opt} tS} \tag{9}$$

where $\dot{m}$ (g) is the water evaporation mass within t time, E_W is evaporation enthalpy of water in PAO/MXene@WN, P_0 (J/m^2/s) is the solar energy density on the surface of the material, C_{opt} (%) is absorbance of the material, S (m^2) refers to the area of the material that receives solar radiation.

4.12 Analysis of Hydrogen Bond Patterns in MXene

A method of quantitative analysis was used to explore the bond mode of hydrogen bonds in MXene. Firstly, the FTIR spectra in the range of 3700 to 3000 cm^{-1} was calculated according to the Savitzky-Golay method. The changes of hydrogen bonds in MXene were then analysed in FTIR spectra fitted via Gaussian distribution function.

5. Figures

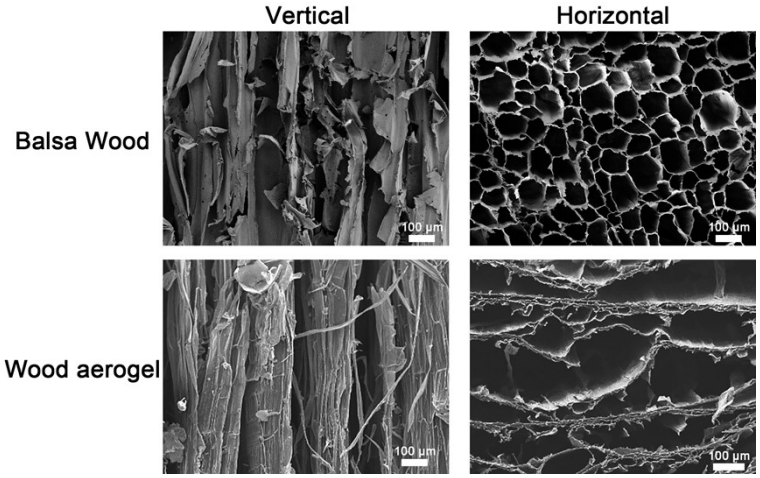

Fig. S1. SEM images of balsa wood and wood aerogel.

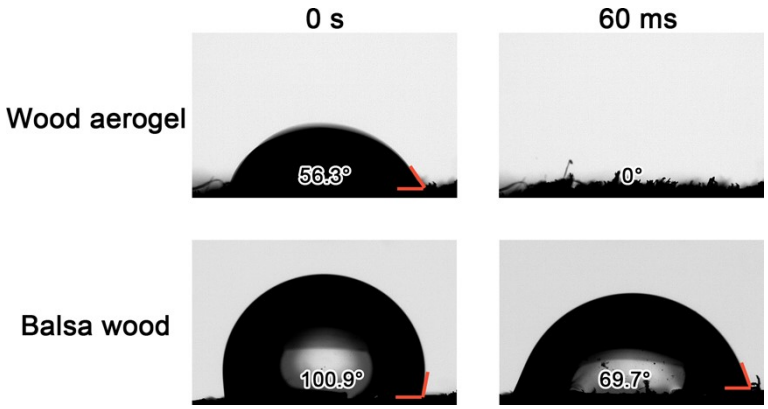

Fig. S2. Water contact angles of wood aerogel and balsa wood.

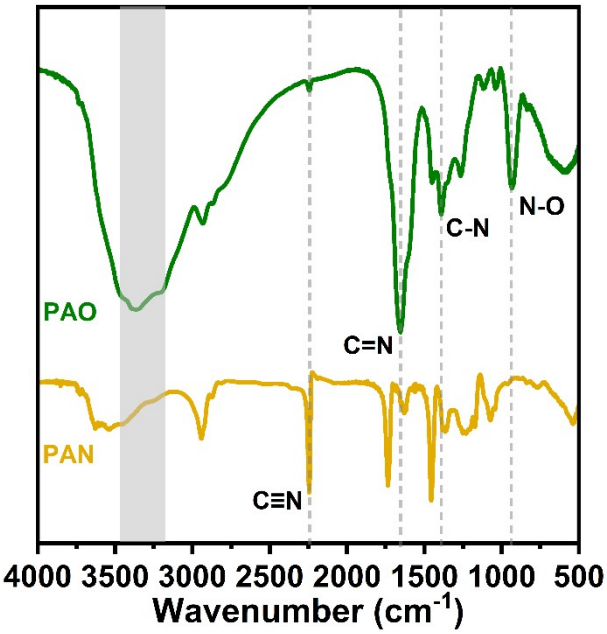

Fig. S3. FTIR of polyacrylonitrile (PAN) and PAO.

The FTIR spectra of PAN possess an obvious characteristic peak at 2244.74 cm^{-1}, which is attributed to the nitrile groups. Following amidoximation, there is the disappearance of the nitrile groups peak, along with the emergence of the C=N (1655.11 cm^{-1}), C-N (1390.42 cm^{-1}) and N-O (933.38 cm^{-1}), indicates the formation of amidoxime groups.

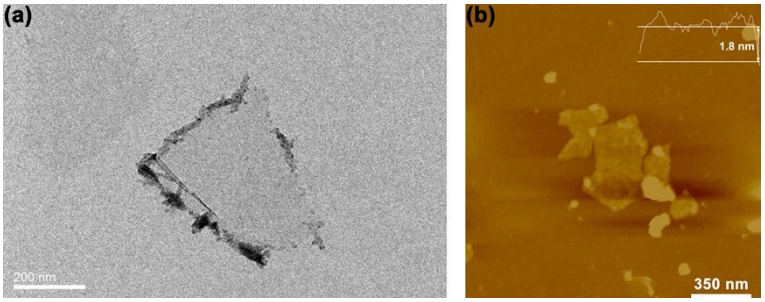

Fig. S4. TEM (a) and AFM (b) images of MXene.

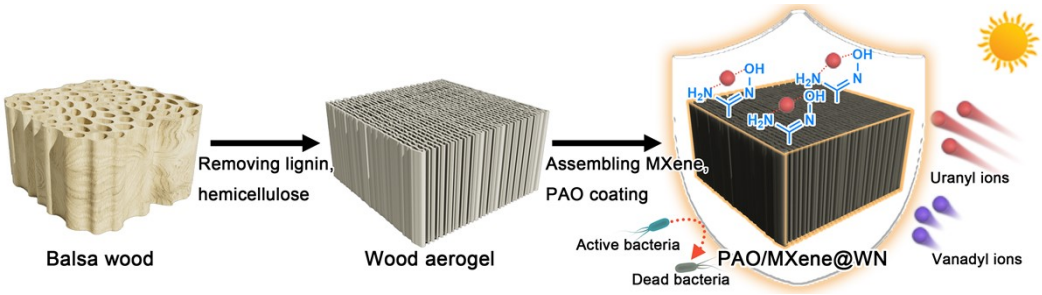

Fig. S5. Preparation process of PAO/MXene@WN.

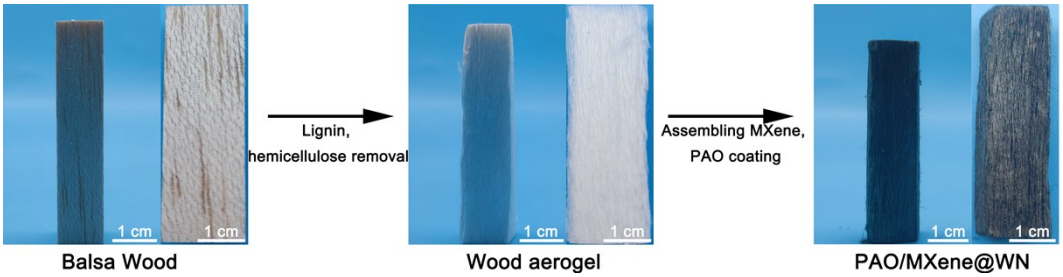

Fig. S6. Digital photographs of balsa wood, wood aerogel and PAO/MXene@WN.

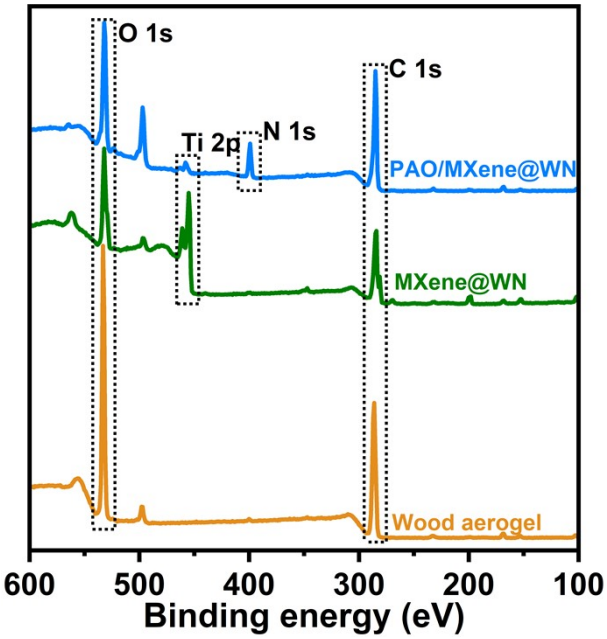

Fig. S7. XPS spectra of wood aerogel, MXene@WN and PAO/MXene@WN.

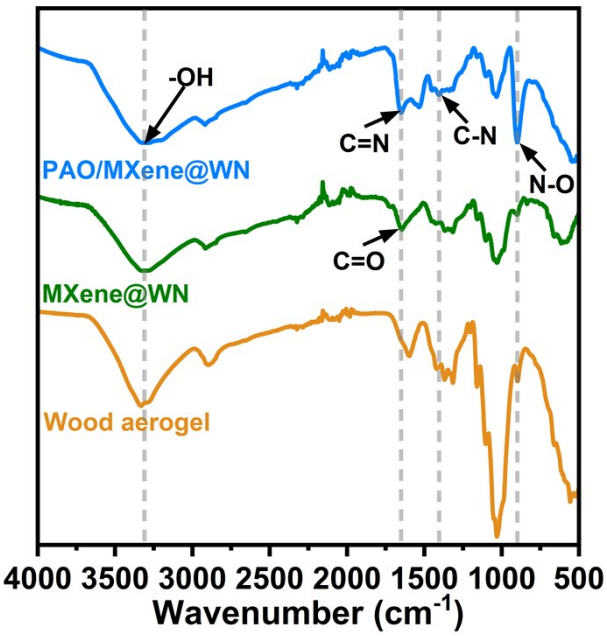

Fig. S8. FTIR spectra of wood aerogel, MXene@WN and PAO/MXene@WN.

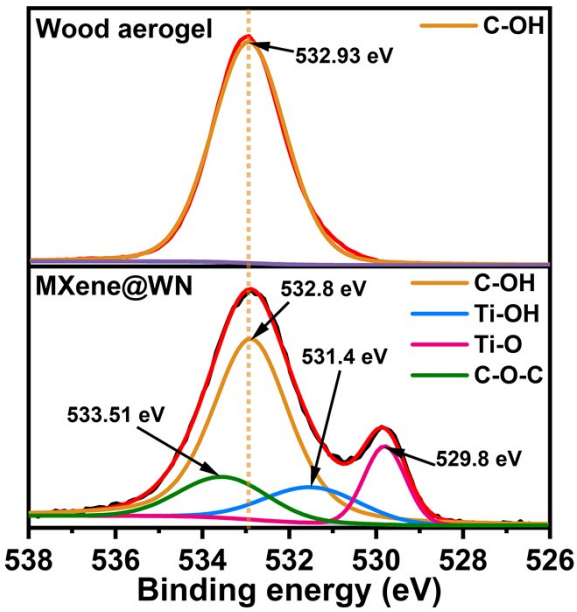

Fig. S9. C 1s XPS spectra of wood aerogel and MXene@WN.

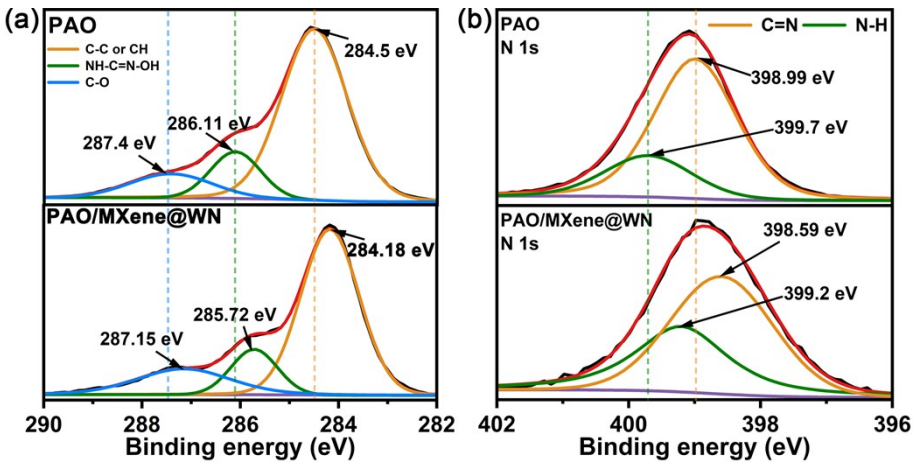

Fig. S10. C 1s (a) and N 1s (b) XPS spectra of PAO and PAO/MXene@WN.

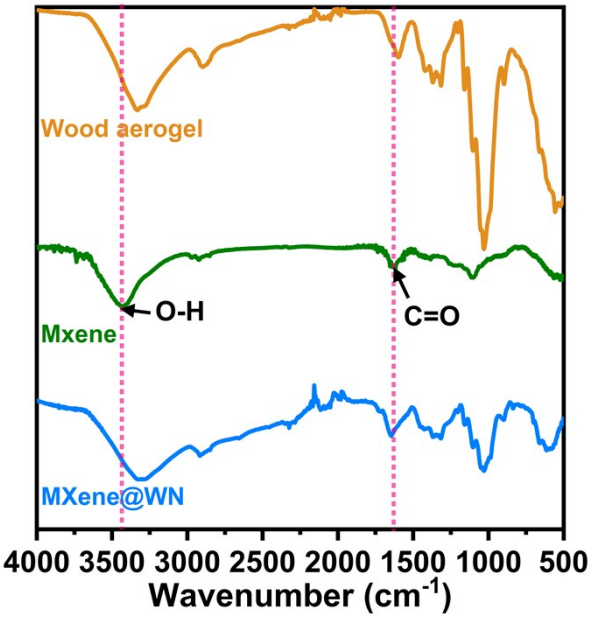

Fig. S11. FTIR spectra of wood aerogel, MXene and MXene@WN.

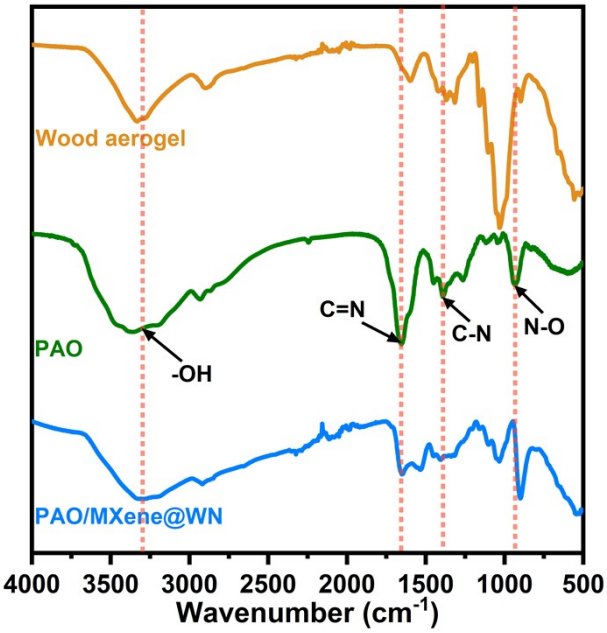

Fig. S12. FTIR spectra of wood aerogel, PAO and PAO/MXene@WN.

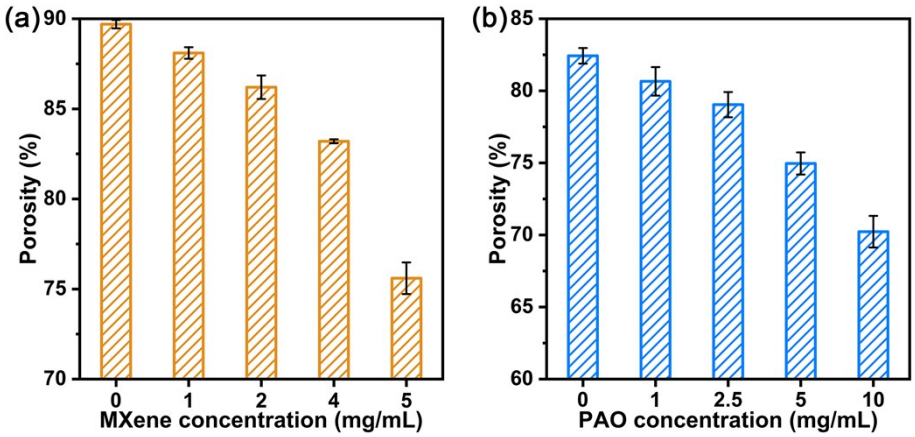

Fig. S13. (a) Effect of different MXene concentrations on porosity of MXene@WN. (b) Effect of different PAO concentrations on porosity of PAO/MXene@WN.

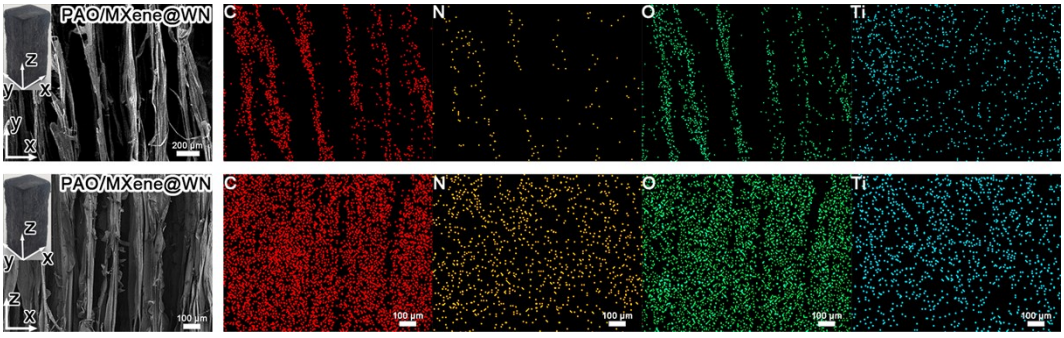

Fig. S14. SEM images and corresponding element mappings of PAO/Mxene@WN.

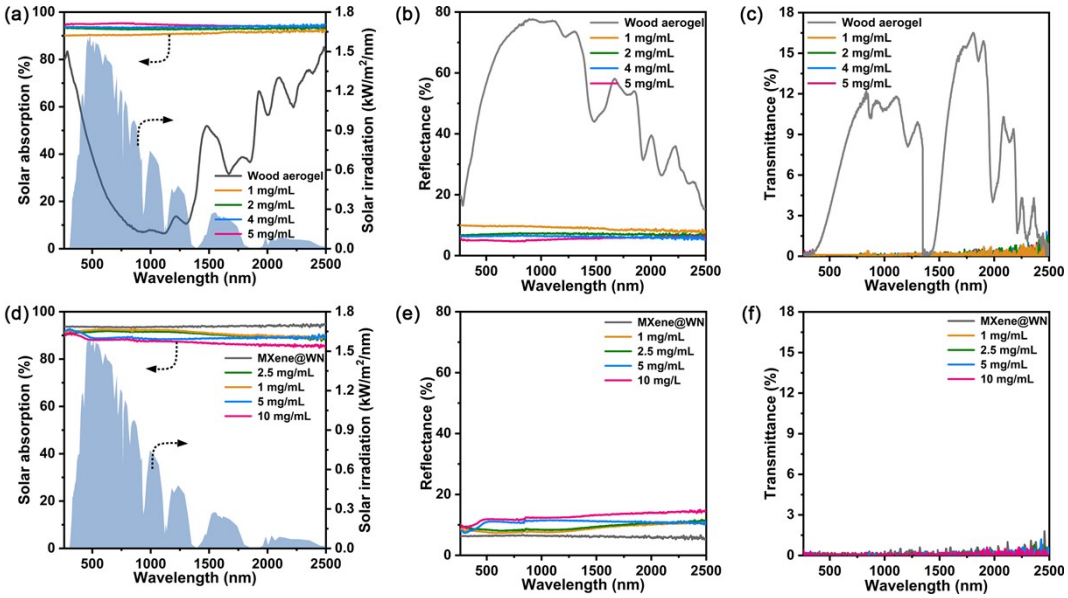

Fig. S15. Solar adsorption (a), reflectance (b) and transmittance (c) of wood aerogel and MXene@WN under different MXene concentrations. Solar adsorption (d), reflectance (e) and transmittance (f) of MXene@WN and PAO/MXene@WN under different PAO concentrations.

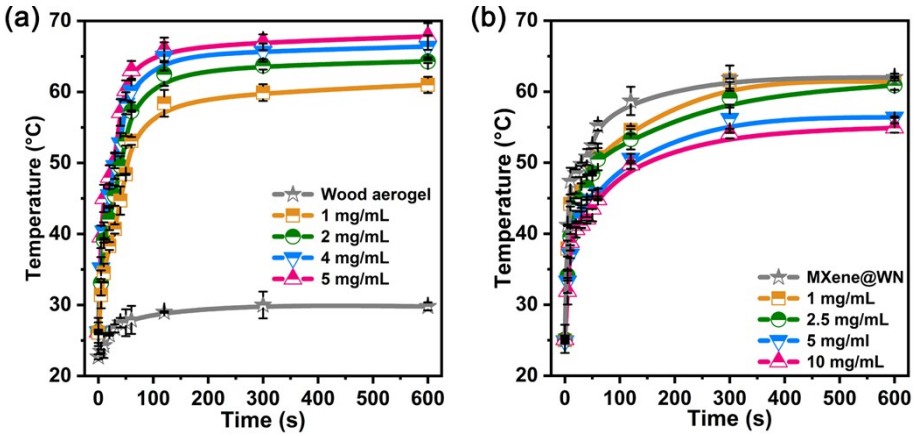

Fig. S16. (a) Surface temperature of wood aerogel and MXene@WN under different MXene concentrations. (b) Surface temperature of MXene@WN and PAO/MXene@WN under different PAO concentrations.

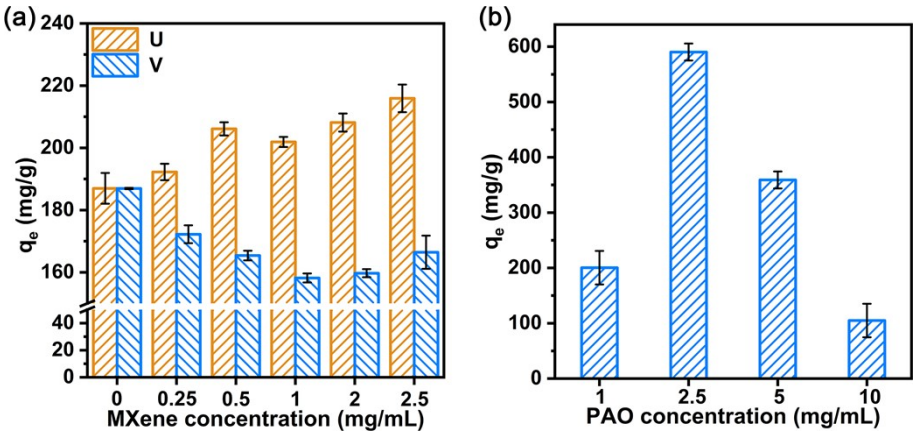

Fig. S17. Uranium adsorption capacity of PAO/Mxene@WN under different MXene (a) and PAO (b) concentrations.

Both uranium adsorption capacity and uranium/vanadium selectivity are improved with the MXene contents. On the one hand, MXene could effectively minimize the spatial configuration changes of amidoxime and maintain a high affinity for uranium due to their strong intermolecular interactions with PAO. On the other hand, the photothermal property of MXene could increase the temperatures which are beneficial for both adsorption capacity as well as uranium/vanadium selectivity.

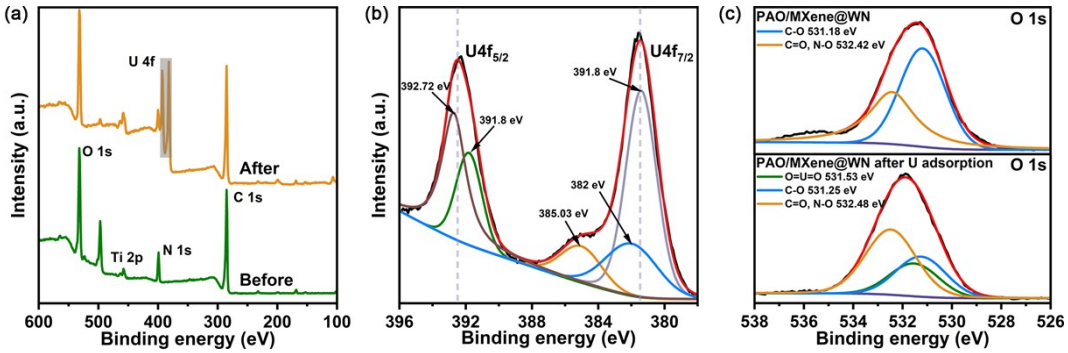

Fig. S18. (a) XPS spectra of PAO/MXene@WN before/after U adsorption. The U 4f (b) and O 1s (c) XPS spectra of PAO/MXene@WN after U adsorption.

Compared with PAO/MXene@WN, the U 4f double peaks are observed in XPS spectrum of PAO/MXene@WN after U adsorption. As shown in **Figure S18b**, the location of the U $4f_{7/2}$, $U4f_{5/2}$ peaks at 381.48 eV and 392.48 eV indicates that existence of U in PAO/MXene@WN. Moreover, the O=U=O group (531.53 eV) appears in O 1 s XPS spectrum from PAO/MXene@WN. Meanwhile, C-O (531.18 eV), C=O and N-O (532.48 eV) attributed to amidoxime group slightly shifted to higher binding energy. These results confirm that the chelation of U with the amidoxime group.

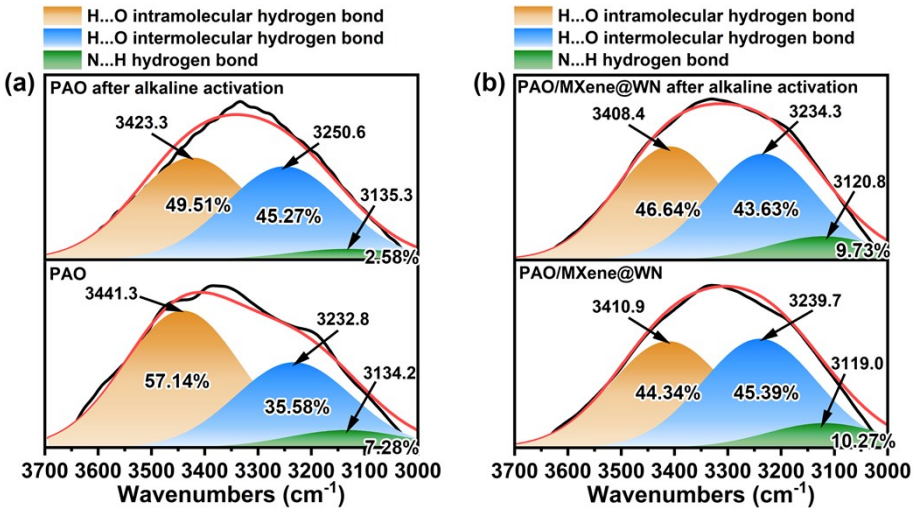

Fig. S19. Gaussian fitting curves of hydrogen bonds insides (a) PAO and (b) PAO/MXene@WN before/after alkaline activation.

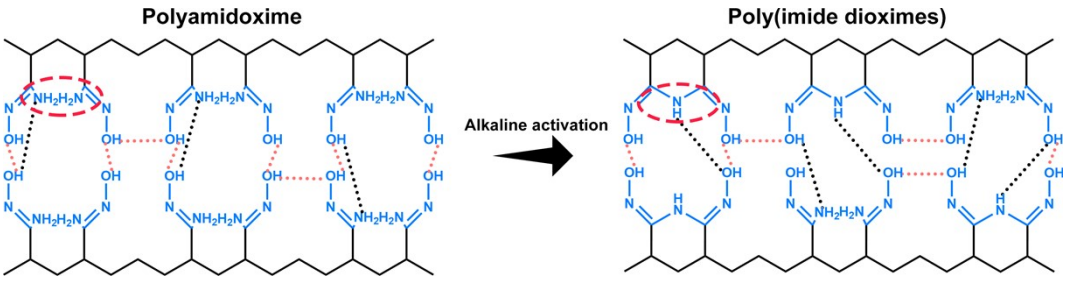

Fig. S20. Schematic diagram of hydrogen bond species.

The -NH_2 from amidoxime tend to form N…H hydrogen bonds with -OH. After alkaline activation for polyamidoxime, the cyclization reaction was occurred, resulting in the conversion of -NH_2 to -NH. Whereas the H…O intermolecular hydrogen bonds readily existed between -NH and OH. Correspondingly, the proportion of H…O intermolecular hydrogen bonds are increased, and the N…H hydrogen bonds fade away.

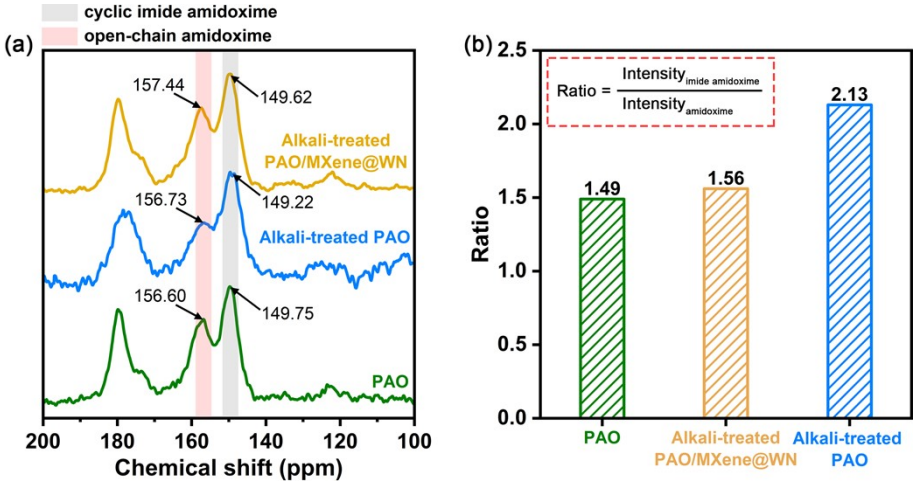

Fig. S21. (a) ^{13}C NMR spectra of PAO, alkali-treated PAO and alkali-treated PAO/MXene@WN. (b) Peak intensity ratio of cyclic imide amidoxime to open-chain amidoxime.

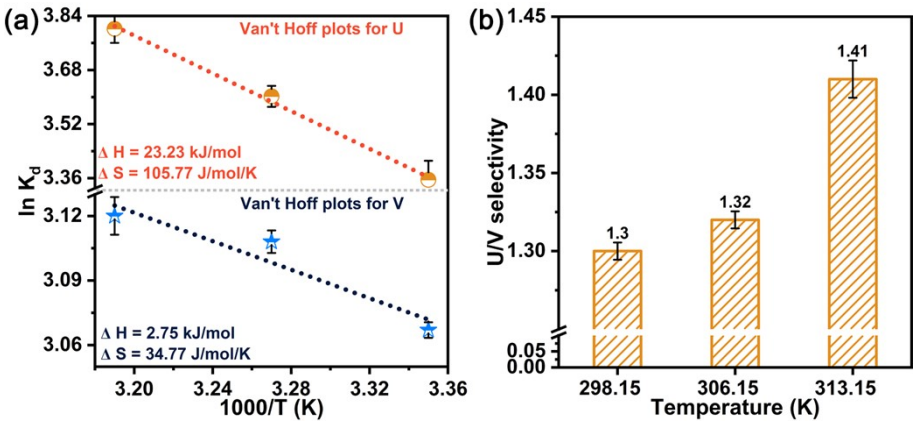

Fig. S22. (a) Van't Hoff plots for uranium and vanadium sorption. (b) Adsorption capacity for uranium and vanadium at different temperatures. The concentrations of uranium and vanadium are 8 mg/L.

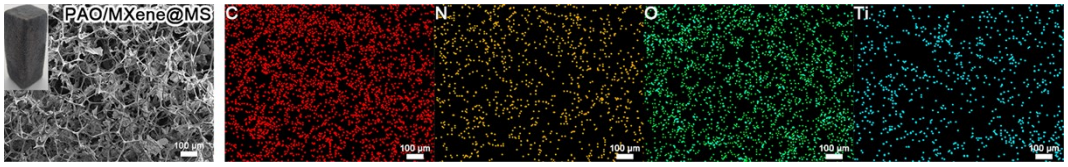

Fig. S23. SEM images and corresponding element mappings of PAO/Mxene@MS.

After modification with MXene and PAO coatings, the melamine sponge still retains its original pore structure, which is beneficial for the transfer of water molecules and uranyl ions.

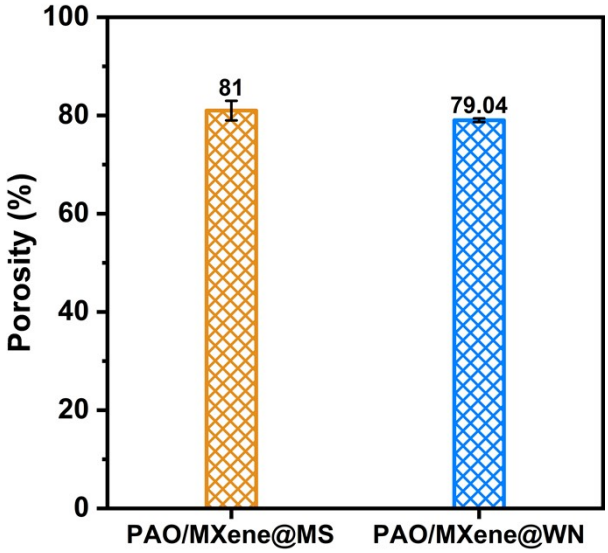

Fig. S24. Porosity of PAO/MXene@MS and PAO/MXene@WN.

PAO/MXene@MS and PAO/MXene@WN all have consistent porosity, which is a prerequisite for exploring differences in contact angle and capillary height.

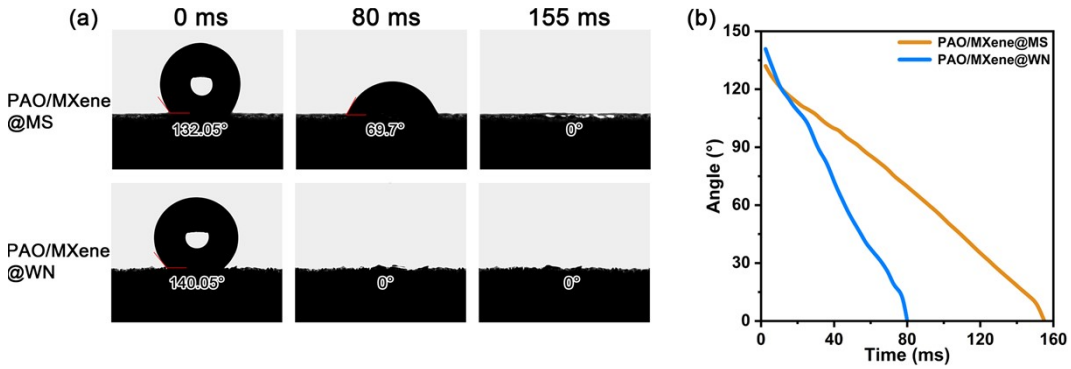

Fig. S25. Digital photographs of glycerol contact angle for PAO/MXene@MS and PAO/MXene@WN (a) as well as corresponding angle as a function of times (b).

To reflect the obvious hydrophilic difference between PAO/MXene@WN and PAO/MXene@MS, the contact angle measurements are conducted using glycerin droplets instead of water droplets. It could be found that there is a significant difference in the time of glycerol penetration between the two, 80 ms for PAO/MXne@WN and 155 ms for PAO/MXene@MS, which suggests that PAO/MXene@WN possesses more excellent hydrophilicity.

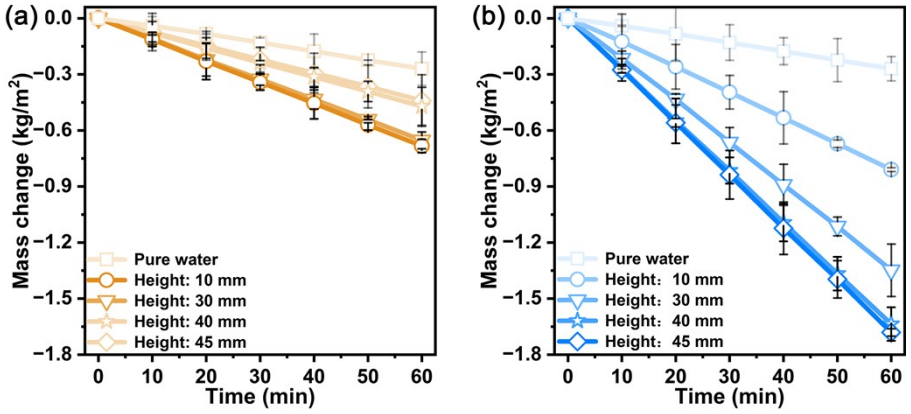

Fig. S26. Mass changes of pure water during evaporation by PAO/MXene@MS (a) and PAO/MXene@WN (b).

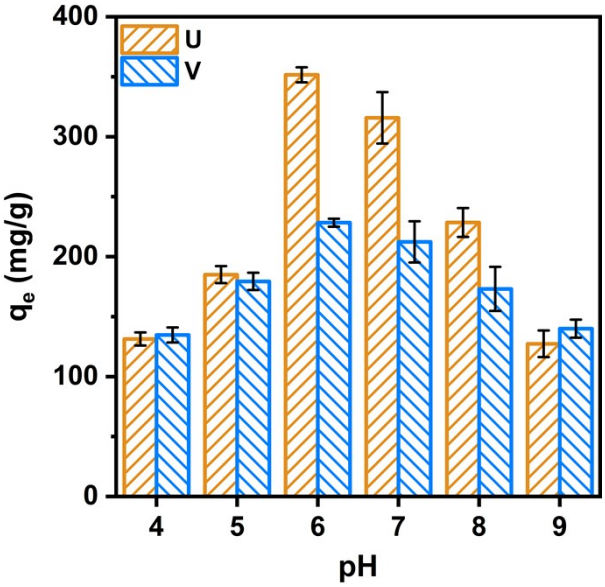

Fig. S27. Effects of pH in solution towards U, V adsorption capacity and U/V selectivity.

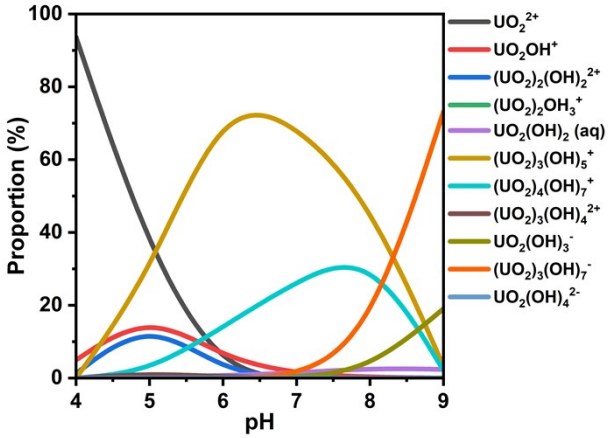

Fig. S28. Distribution of uranyl ions species at different pH values (simulated by Visual MINEQL, NIST database. UO_2^{2+} concentration: 8 mg/L, temperature: 298.15 K).

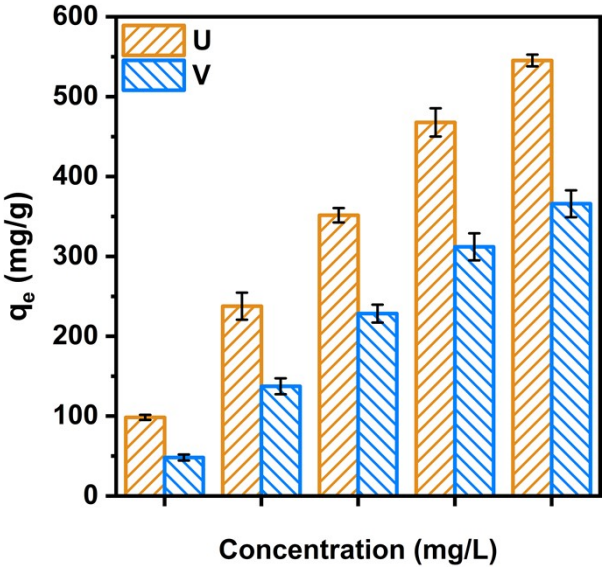

Fig. S29. Effects of ions concentration towards U, V adsorption capacity and U/V selectivity.

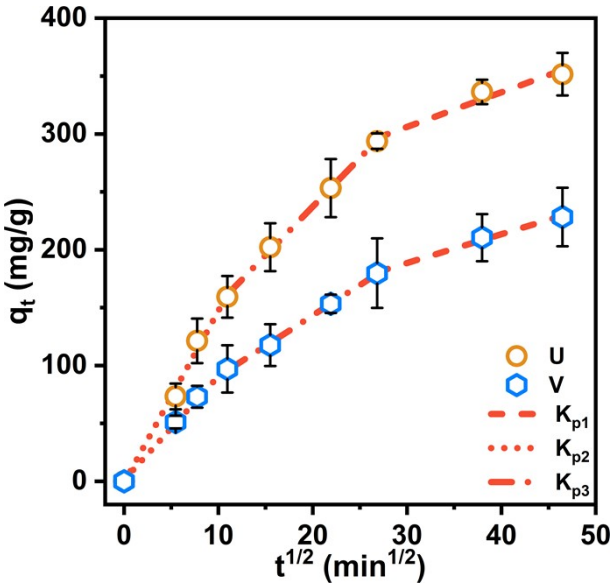

Fig. S30. Intraparticle diffusion kinetics of U, V for PAO/MXene@WN. (U, V concentration: 8 mg/L, volume: 1 L, temperature: 298.15 K, simulated solar intensity: 1 kW/m^2)

To reveal why PAO/MXene@WN has a high U/V selectivity, we investigated the adsorption processes of uranium and vanadium by analyzing the intraparticle diffusion kinetics[5] (**Table S3**). The typical intraparticle diffusion models could be divided into three stages: 1) hydration layers are formed on the surface of adsorbents and the ions are adsorbed while the rate constants are named as Kp_1; 2) ions gradually diffuse from the outer layer to the inner layer of adsorbent, during which the rate constants are Kp_2; 3) the third step (Kp_3) is that the ions chelate with the adsorption sites. The Kp_1, Kp_2 of uranium are greater than that of the vanadium, indicating that PAO/MXene@WN has a stronger affinity for uranium.

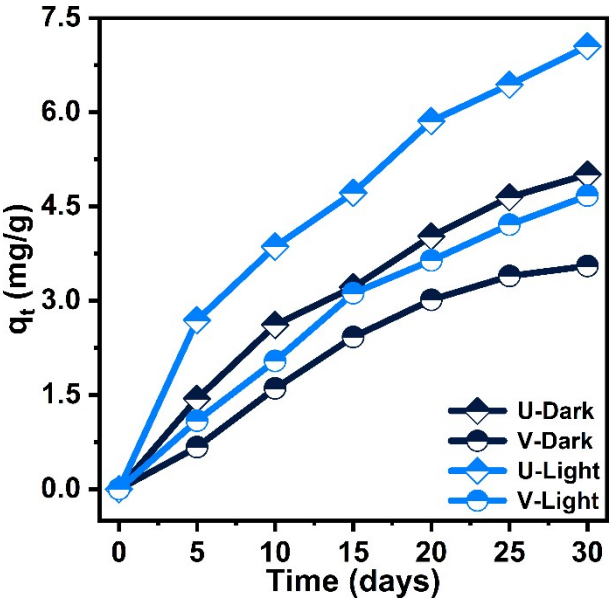

Fig. S31. Adsorption capacity for U, V of PAO/MXene@WN in seawater under dark/light conditions.

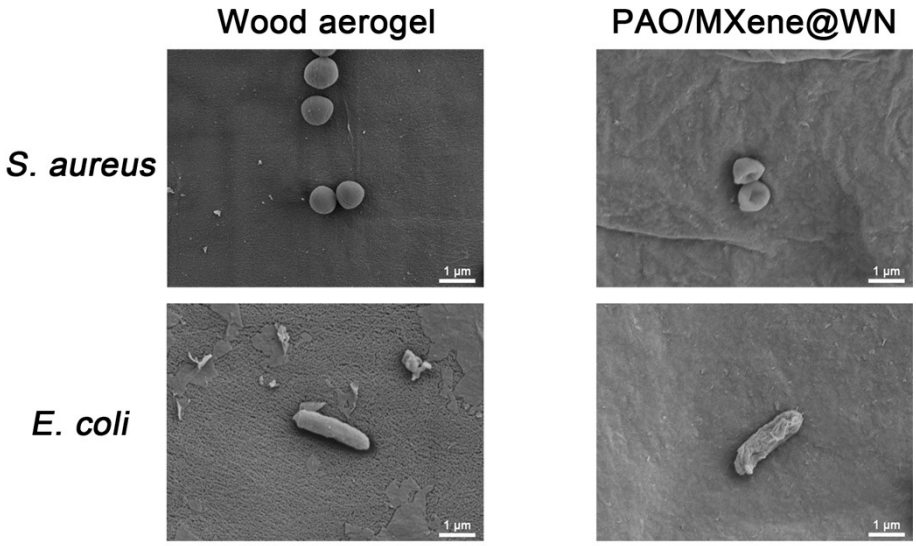

Fig. S32. SEM images of bacteria contacting with wood aerogel and PAO/MXene@WN.

6. Tables

Table S1. Thermodynamics parameters for ions sorption of PAO/Mxene@WN.

	ΔH (kJ/mol)	ΔS (Jmol/K)	ΔG (kJ/mol)		
Uranium	23.23	105.77	298.15 K	306.15 K	313.15 K
			-8.31	-9.15	-9.89
Vanadium	2.75	34.77	298.15 K	306.15 K	313.15 K
			-7.62	-7.89	-8.14

Table S2. Distribution proportion of uranyl ions species at different pH values.

pH / Ion species	4	5	6	7	8	9
UO_2^{2+}	93.663%	33.868%	1.005%	0.021%	≈ 0%	≈ 0%
UO_2OH^+	4.968%	18.177%	5.464%	1.141%	0.218%	0.019%
$(UO_2)_2(OH)_2^{2+}$	1.241%	16.475%	1.477%	0.064%	≈ 0%	≈ 0%
$(UO_2)_2OH_3^+$	0.114%	0.148%	≈ 0%	≈ 0%	≈ 0%	≈ 0%
$UO_2(OH)_2$ (aq)	≈ 0%	0.225%	0.68%	1.422%	2.71%	2.373%
$(UO_2)_3(OH)_5^+$	≈ 0%	28.096%	76.976%	70.268%	48.656%	3.269%
$(UO_2)_4(OH)_7^+$	≈ 0%	1.697%	14.033%	26.78%	35.343%	2.08%
$(UO_2)_3(OH)_4^{2+}$	≈ 0%	1.315%	0.356%	0.032%	≈ 0%	≈ 0%
$UO_2(OH)_3^-$	≈ 0%	≈ 0%	≈ 0%	0.114%	2.175%	19.059%
$(UO_2)_3(OH)_7^-$	≈ 0%	≈ 0%	≈ 0%	0.157%	10.893%	73.186%
$UO_2(OH)_4^{2-}$	≈ 0%	≈ 0%	≈ 0%	≈ 0%	≈ 0%	0.014%

Table S3. Parameters of intraparticle diffusion model.

	K_{p1}	R_{p1}^2	K_{p2}	R_{p2}^2	K_{p3}	R_{p3}^2
Uranium	14.8262	0.99237	8.3964	0.99877	2.98522	0.96441
Vanadium	8.95541	0.99747	5.25935	0.99846	2.48538	0.99424

Table S4. Comparison of distribution coefficient among state-of-the art adsorbents.

Adsorbents	Distribution coefficient (K_d, 10^5 mL/g)	Conditions	Ref.
This work	5.43	C_0 = 0.33 ppm; V = 1 L; m = 5 mg	/
DC-PAO[a]	2.4	C_0 = 0.33 ppm; V = 2 L; m = 10 mg	[6]
PAO PNMs[a]	1.99	C_0 = 0.33 ppm; V = 1 L; m = 5 mg	[7]
CPAO[a]	1.95	C_0 = 80 ppm; V = 0.1 L; m = 20 mg	[8]
PIDO NF[a]	1.09	C_0 = 0.33 ppm; V = 10 L; m = 15 mg	[9]
PAO/GO[a]	0.529	C_0 = 0.33 ppm; V = 1 L; m = 5 mg	[10]
Zn^{2+}-PAO hydrogel[a]	0.298	C_0 = 32 ppm; V = 2 L; m = 10 mg	[11]
FF-Cu_2O/AO[b]	1.01	C_0 = 0.33 ppm; V = 1 L; m = 5 mg	[12]
AFC microspheres[b]	0.343	C_0 = 0.33 ppm; V = 1 L; m = 180 mg	[13]
PEI-AOBS-2[b]	0.326	C_0 = 93.75 ppm	[14]
GDC[b]	0.04	C_0 = 10 ppm; V = 0.5 L; m = 30 mg	[15]

COF-HHTF-AO[c]	4.3	C_0 = 0.33 ppm	[16]
JUC-505-AO[c]	0.74	C_0 = 3 ppm; V = 1 L; m = 1000 mg	[17]
tBPF-AO[c]	0.202	C_0 = 80 ppm	[18]
AO-NPCDP[c]	0.184	C_0 = 20 ppm	[19]
NH_2@AO-PLRMS[d]	1.88	C_0 = 0.33 ppm; V = 1 L; m = 5 mg	[20]
CID NFs[d]	1.46	C_0 = 0.33 ppm; V = 1 L; m = 20 mg	[21]
AO-OpNpNc[d]	0.36	C_0 = 0.33 ppm; V = 60 L; m = 5 mg	[22]
MAH-co-AO[d]	0.33	C_0 = 4.124 ppm; V = 1 L; m = 400 mg	[23]
UiO-66-NH-(AO)[c]	0.88	C_0 = 0.33 ppm; V = 1 L; m = 20 mg	[24]
MIL-101-AO[c]	0.53	C_0 = 1 ppm; V = 0.05 L; m = 5 mg	[25]
ZIF-90-OM[c]	0.46	C_0 = 10 ppm; V = 1 L; m = 100 mg	[26]
PCN-222-AO[c]	0.26	C_0 = 10 ppm; V = 1 L; m = 200 mg	[27]
ZIF-90-AO[c]	0.22	C_0 = 10 ppm; V = 1 L; m = 100 mg	[28]
AO-PIM-1[c]	0.52	C_0 = 0.33 ppm; V = 1 L; m = 5 mg	[29]

HSMSMs-AO[e]	2.14	C_0 = 50 ppm; V = 0.25 L; m = 5 mg	[30]
AO-C3N4[e]	1.61	C_0 = 3.3 ppb; V = 20 L; m = 5 mg	[31]
Fe3O4/P(GMA-AA-MMA)[e]	1.5	C_0 = 0.5 ppm; V = 0.025 L; m = 10 mg	[32]
MPH beads[e]	0.82	C_0 = 21.6 ppm	[33]
SiO2-AO[e]	0.31	C_0 = 50 ppm; V = 0.06 L; m = 30 mg	[34]

a, PAO-based adsorbents; b, biomass-based adsorbents; c, porous skeleton polymer-based adsorbents; d, macromolecule polymer-based adsorbents; e, other adsorbents.

7. References

[1] G. Kresse, J. Furthmüller, *Comput. Mater. Sci.* **1996**, 6, 15.

[2] J. P. Perdew, K. Burke, M. Ernzerhof, *Phys. Rev. Lett.* **1996**, 77, 3865.

[3] P. E. Blöchl, *Phys. Rev. B* **1994**, 50, 17953.

[4] S. Grimme, *J. Comput. Chem.* **2006**, 27, 1787.

[5] D. Ji, Y. Liu, H. Ma, Z. Bai, Z. Qiao, D. Ji, C. Yan, Y. Yan, H. Wu, *ACS Sustainable Chem. Eng.* **2022**, 10, 11990.

[6] N. Wang, X. M. Zhao, J. W. Wang, B. J. Yan, S. X. Wen, J. C. Zhang, K. Lin, H. Wang, T. Liu, Z. Z. Liu, C. X. Ma, J. B. Li, Y. H. Yuan, *Adv. Sci.* **2021**, 8.

[7] S. Shi, Y. Qian, P. Mei, Y. Yuan, N. Jia, M. Dong, J. Fan, Z. Guo, N. Wang, *Nano Energy* **2020**, 71, 104629.

[8] Y. Xu, J. Yu, J. Zhu, Q. Liu, H. Zhang, J. Liu, R. Chen, Y. Li, J. Wang, *Appl. Catal. B-Environ.* **2022**, 316, 121677.

[9] D. Wang, J. Song, J. Wen, Y. Yuan, Z. Liu, S. Lin, H. Wang, H. Wang, S. Zhao, X. Zhao, M. Fang, M. Lei, B. Li, N. Wang, X. Wang, H. Wu, *Adv. Energy Mater.* **2018**, 8, 1802607.

[10]T. Liu, R. Q. Zhang, M. W. Chen, Y. J. Liu, Z. J. Xie, S. Tang, Y. H. Yuan, N. Wang, *Adv. Func. Mater.* **2022**, 32.

[11]B. Yan, C. Ma, J. Gao, Y. Yuan, N. Wang, *Adv. Mater.* **2020**, 32, 1906615.

[12]Y. Pu, T. Qiang, L. Ren, *Desalination* **2022**, 531, 115721.

[13]S. C. Liu, M. B. Wu, H. Ye, L. Liu, L. L. Ma, J. M. Yao, *Chem. Eng. J.* **2021**, 426.

[14]Y. Wang, Z. Lin, J. Zhu, J. Liu, J. Yu, Q. Liu, R. Chen, Y. Li, J. Wang, *J. Hazard. Mater.* **2022**, 437, 129407.

[15]N. Li, L. Yang, D. Wang, C. Tang, W. Deng, Z. Wang, *Environ. Sci. Technol.* **2021**, 55, 9181.

[16]G. Cheng, A. Zhang, Z. Zhao, Z. Chai, B. Hu, B. Han, Y. Ai, X. Wang, *Sci. Bull.* **2021**, 66, 1994.

[17]Z. Li, R. Zhu, P. Zhang, M. Yang, R. Zhao, Y. Wang, X. Dai, W. Liu, *Chem. Eng. J.* **2022**, 434, 134623.

[18]R. Leng, Y. Sun, C. Wang, Z. Qu, R. Feng, G. Zhao, B. Han, J. Wang, Z. Ji, X. Wang, *Environ. Sci. Technol.* **2023**, 57, 9615.

[19]Y. Sun, R. Leng, X. Ma, J. Zhang, B. Han, G. Zhao, Y. Ai, B. Hu, Z. Ji, X. Wang, *Chem. Eng. J.* **2023**, 459, 141687.

[20]X. Bai, Y. Wang, H. Li, X. Tian, Y. Ma, J. Pan, *J. Hazard. Mater.* **2021**, 419, 126398.

[21]C. Huang, L. Xu, X. Xu, L. Ma, H. Bao, J. Liao, J. Wang, J. Han, G. Xu, D. Huang, B. Ye, H. Zhang, M. Wu, X. Zhao, H. Ma, *Chem. Eng. J.* **2022**, 443, 136312.

[22]X. Xu, L. Xu, J. Ao, Y. Liang, C. Li, Y. Wang, C. Huang, F. Ye, Q. Li, X. Guo, J. Li, H. Wang, S. Ma, H. Ma, *J. Mater. Chem. A* **2020**, 8, 22032.

[23]L. Yang, L. Bi, Z. Lei, Y. Miao, B. Li, T. Liu, W. Wu, *Polymers*, **2018**, 10(3), 236..

[24]L. Ma, J. Gao, C. Huang, X. Xu, L. Xu, R. Ding, H. Bao, Z. Wang, G. Xu, Q. Li, P. Deng, H. Ma, *ACS ACS Appl. Mater. Interfaces* **2021**, 13, 57831.

[25]L. Liu, Y. Fang, Y. Meng, X. Wang, F. Ma, C. Zhang, H. Dong, *Desalination* **2020**, 478, 114300.

[26]D. Mei, H. Li, L. Liu, L. Jiang, C. Zhang, X. Wu, H. Dong, F. Ma, *Chem. Eng. J.* **2021**, 425, 130468.

[27]C. Bi, C. Zhang, W. Xu, F. Ma, L. Zhu, R. Zhu, Q. Qi, L. Liu, J. Bai, H. Dong, *Desalination* **2023**, 545, 116169.

[28] D. Mei, L. Liu, H. Li, Y. Wang, F. Ma, C. Zhang, H. Dong, *J. Hazard. Mater.* **2022**, 422, 126872.
[29] L. S. Yang, H. Y. Xiao, Y. C. Qian, X. L. Zhao, X. Y. Kong, P. Liu, W. W. Xin, L. Fu, L. Jiang, L. P. Wen, *Nat. Sustainability* **2022**, 5, 71.
[30] Q. Chen, X. Xue, Y. Liu, A. Guo, K. Chen, J. Yin, F. Yu, H. Zhu, X. Guo, *J. Hazard. Mater.* **2022**, 438, 129524.
[31] K. Yu, Y. Li, X. Cao, R. Wang, L. Zhou, L. Wu, N. He, J. Lei, D. Fu, T. Chen, R. He, W. Zhu, *J. Hazard. Mater.* **2023**, 460, 132356.
[32] D. Yuan, L. Chen, X. Xiong, L. Yuan, S. Liao, Y. Wang, *Chem. Eng. J.* **2016**, 285, 358.
[33] Y. Zhou, J. Yang, N. Zhou, H. Hao, X. Jiang, F. Lei, K. Shi, Y. Zhao, G. Zhou, T. Liu, S. Xing, *Chem. Eng. J.* **2023**, 471, 144647.
[34] M. Ahmad, J. Wang, Z. Yang, Q. Zhang, B. Zhang, *Chem. Eng. J.* **2020**, 389, 124441.